SLAC-J-ICFA-20
Spring 2000
SLAC-R-651

HOME PAGE

http://www.slac.stanford.edu/pubs/icfa/

ICFA INSTRUMENTATION BULLETIN*

The publication of the ICFA Instrumentation Bulletin is an activity of the Panel on Future Innovation and Development of ICFA (International Committee for Future Accelerators).

Volume 20

• Spring 2000 Issue

* Supported by the Department of Energy, contract DE-AC03-76SF00515.

ICFA INSTRUMENTATION BULLETIN

The publication of the ICFA Instrumentation Bulletin is an activity of the Panel on Future Innovation and Development of ICFA (International Committee for Future Accelerators). The Bulletin reports on research and progress in the field of instrumentation with emphasis on application in the field of high-energy physics. It encourages issues of generic instrumentation.

Publisher : Stanford Linear Accelerator Center
SLAC Publications Department
Stanford, CA 94309, U.S.A.

Editor : J. Va'vra

Web Technical Adviser : J. Schwiening

The views expressed in this Bulletin do not necessarily represent those of the ICFA Panel or the editor. In all cases, the authors are responsible for their manuscripts. The printed version is mailed out in limited numbers to institutions on the SLAC Instrumentation mailing list. Issues of the ICFA Instrumentation Bulletin are accessible electronically on our Web site:

http://www.slac.stanford.edu/pubs/icfa/

Cover: The illustration depicts L. J. Waghenaer's marine atlas, "The Mariner's Mirror," published in 1588. Lucas Janszoon Waghenaer was born in Holland in the 1530s. He became a famous ship pilot in his time. In 1584, he published the atlas ("Spieghel der Zeevaerdt") which was greatly valued among mariners for centuries. This was not due only to the map content, but also to the detailed knowledge of navigation techniques of that time. The atlas, as it appears on our page, is the same one used for the Dutch to English translation.

Conference List

- ICFA School on Instrumentation in Particle Physics, Near Cape Town, South Africa, March 26 to April 6, 2001.

- RICH 2001 Workshop, Pylos, Greece, September 3-7, 2001.

Table of Contents

FRONT END ELECTRONICS DEVELOPMENTS FOR PARTICLE PHYSICS: PARADIGM OR PARADOX?

G. Hall

Blackett Laboratory, Imperial College, London SW7 2AZ, UK

g.hall@ic.ac.uk

Abstract

Recent years have seen much dedicated work on front end electronics for hadron colliders, with an strong emphasis on radiation hardness and low cost. This has been challenging for a number of reasons, some of which are discussed further below. The developments also suggest opportunities and constraints for the development of such electronics in the future.

1. Introduction

Reviewing progress in front end electronics is intimidating because it covers a wide range of components, techniques ,and technologies. Some recent developments, particularly those for the Large Hadron Collider, have been under way for almost a decade and are still not complete, which gives an indication of the magnitude of some challenges. It is interesting to ask why this is so.

It is sometimes valuable to look backwards as well as forwards. During the last decade many different technologies have been investigated and some have been discarded, while others have perhaps matured faster than expected. This article surveys some selected areas where a lot of attention has been focussed and offers comments on what has been achieved, and where some developments may go in the future.

Do developments focussed mainly on hadron collider operation offer any relevant lessons for other experiments in particle physics? Similar systems are now also often applied in other fields of science, so lessons learned from particle physics may be relevant elsewhere.

This paper addresses general issues, without providing details of solutions; many of these can be found in Refs. [1-4].

2. Hadron collider electronic requirements

Since most developments presently underway can be traced back to the special needs for electronics for the SSC and subsequently the LHC, the most relevant LHC operational parameters as seen by one general purpose detector, CMS, are summarised in Table 1. There are only minor differences for ATLAS, except that heavy ion operation is not planned.

Almost completely hermetic, general purpose detectors operated with high efficiency to detect rare events were recognised to be essential for TeV physics, and it was understood very early that radiation tolerance would be one of the biggest problems, supplemented by very high readout rates. The innermost regions of the experiments are subject to high particle fluxes and thus radiation levels. The large majority of the sensor technologies in use for particle physics in the 1980s were known either to be problematic for application in tracking systems and electromagnetic calorimeters, e.g., silicon, crystalline and plastic scintillators, or completely excluded, e.g., gas detectors such as TPCs or large volume drift chambers.

These challenges motivated dedicated R&D programmes; most emphasised sensors, although several projects recognised that compatible electronics would have to be developed in parallel to match operational conditions.

Table 1		
particles	pp	Pb-Pb
Luminosity	10^{34} cm^{-2}.s^{-1}	10^{27} cm^{-2}.s^{-1}
Average integrated luminosity	5×10^{40} cm^{-2}.y^{-1}	10^{33} cm^{-2}. y^{-1} ?
CM energy	14 TeV	5.5 TeV/N
$\sigma_{inelastic}$	~70mb	~6.5 b
Interactions/bunch	~20	0.001
Tracks/unit rapidity interval/crossing	~140	3000-8000
beam crossing rate	40MHz	8MHz
L1 trigger delay	≈3.2μsec	≈3.2μsec
L1 trigger rate	≤100kHz	< 8kHz

The LHC experiments are enormous in comparison with previous generations and most sub-systems have huge numbers of readout channels. The sub-detector systems are highly distributed and remote, and inaccessible for long periods, demanding high reliability. The very large data volumes and minimal deadtime requirement, require fast front end data links and efficient processing. Many secondary specifications are *extremely* demanding, such as temperature stability, magnetic field operation, radiation tolerance, and material budget reduction.

High speed signal processing has major implications for front-end power, signal-to-noise ratios and overall performance. The high charged particle and neutron fluences must be prevented from degrading performance but also raise issues of qualification, reliability, and maintenance. On-line reduction of first level data is mandatory.

Radiation concerns apply throughout the experiment caverns where, even at the walls, low ionising doses but significant neutron fluences are expected. These are a concern for support electronics, like power supplies, or computing and control components. High magnetic fields are used and significant stray fields are anticipated.

3 Requirements for different detectors

Colliding beam experiments are all constructed in a generally similar way and it may be helpful to identify the main parameters defining the various electronic systems. Descriptions like "low power" and "low radiation levels" can mean quite different things in different sub-detectors.

For the benefit of the general reader, tracking systems surround the beam pipe to measure charged particle trajectories, calorimeter systems follow, with high density, large volume absorbers as detectors, and, finally, detectors on the outside measure the locations of penetrating muons. The surface area of each system therefore usually grows with distance from the beam but the density of electronics usually decreases.

Requirements for tracking are high spatial precision on particle trajectories but limited energy precision. Detectors are highly granular, leading to enormous channel counts. The dynamic range of signals is limited to a few bits since highly linear responses are not needed for the full range of signal amplitudes; of more importance is the ability to distinguish genuine signals from background, so low noise readout has high priority. This must be achieved using a few mW/channel with fast pulse shaping and in multi-Mrad radiation levels because of proximity to the beam. Power constraints are imposed by the need for a low material budget to minimise photon conversions and electron bremsstrahlung, so cables and cooling mass must be minimised.

Calorimeter detectors aim for very high energy resolution over a very large dynamic range; with very stable performance over time. The detector absorbs most hadrons, so it usually shields the electronics and radiation levels typically up to ~1Mrad. Removing heat is still a problem, both in the region of the sensor and from ohmic heating in cables.

Muon systems are spread over large areas. Although the spatial precision required is moderate compared to the trackers, it must be achieved over much larger areas with small systematic effects, so alignment and stability are vital features. Particle counting rates are high when integrated over the large areas over which signals are sensed. Radiation levels are low but heavy reliance on

programmable logic implemented in standard commercial parts raises difficult questions of qualification and maintenance.

Generic LHC readout system

All systems require amplification and filtering, analogue to digital conversion (at least one bit!) and storage prior to data readout initiated by a trigger. Pipeline memories are widely utilised but they appear in different forms, either analogue or digital, and in different locations, either on or off the front end. In all cases, data must be associated to the correct beam crossing and the complexity of this requirement is influenced by the point at which data are digitised and compressed or "sparsified."

Two variants of a typical LHC readout system are illustrated in fig.1; other variants are possible. They demonstrate that many LHC systems are rather complex. Not only do front-end chips embody amplification and bandwidth limiting filters but many of them include digital control logic and, often, other analogue or digital processing functions.

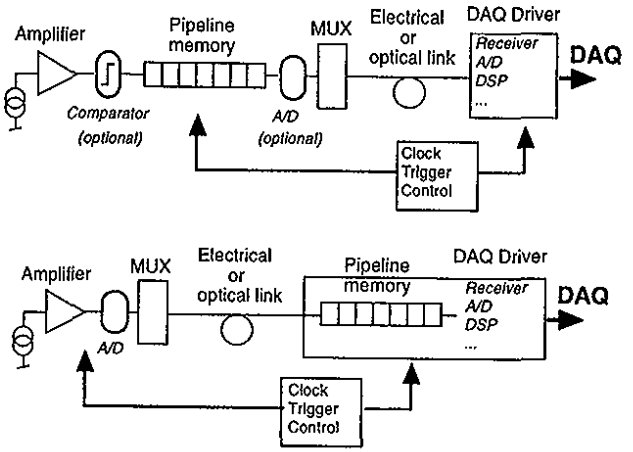

Fig. 1. Two variants of generic LHC front-end readout systems.

Systems should be able to handle incoming signals while processing data from previous events at up to the maximum trigger rate. This is provided by circular pipeline architectures which sample signals at the machine clock frequency and pointers circulate, marking and skipping cells which contain data awaiting readout. This is a classical queueing problem but logic emulation is needed to compute losses in detail. Poisson fluctuations in trigger arrival mean that practical buffer depths cannot guarantee unlimited operation without overflows; in practice data losses of ~1% are tolerated.

First level triggers are generated by fast readout of limited precision data from calorimeter and muon systems. This is the first level of data rejection. Subsequently, increasingly selective rejection of "uninteresting" events will take place using more precise data from all sub-systems so that eventually data can be written to permanent storage devices at the maximum permitted rate of ~100Hz.

4. Radiation tolerance of electronics

Radiation hardness is one reason for lengthy LHC electronic developments, since at the outset few people had experience of radiation hard electronic technologies. This applied also to detectors, but much of the detector manufacturing was done in-house (gas detectors) or with

relatively small, specialised companies (silicon or scintillators) who were willing to prototype and even modify existing technologies at modest cost. This was much less possible for electronics.

For convenience, one can classify electronics as COTS (Commercial Off The Shelf) components, including programmable logic (FPGAs), or Application Specific Integrated Circuits (ASICs). The radiation tolerance of each strongly depends on technology and application, e.g., current density employed. The principal origins of damage are ionisation charge in oxides and atomic displacement damage to substrates.

CMOS circuits are neutron hard but ionising dose sensitive. Charge created by ionisation builds up in the oxide near to the silicon-oxide interface and induces shallow surface charge layers or creates interface states which influence device operation. Typical consequences are gate threshold voltage shifts, increased noise, inter-device leakage currents and latch-up caused by creation of parasitic devices, which can be fatal. Conventional processes, and COTS components made in them, may have very low tolerance, even a few krad.

A further phenomenon in logic circuits, increasingly studied as other effects are better understood, is Single Event Upset (SEU), in which knock-on ions deposit heavy ionisation in a small volume near a sensitive circuit node and cause a change of logic state. Even in low-flux conditions, operational errors in control circuits could magnify the importance of SEU.

Bipolar circuits are affected by atomic displacement in the body of the device which increases carrier recombination in the base of transistors giving rise to gain and matching degradation. These effects can also result from oxide charging in bipolar ICs. Low-energy neutrons diffusing throughout the LHC caverns will be a significant damage source, as well as hadrons from beam collisions. Discrete bipolar circuits usually withstand high exposures, and the few integrated circuit processes in use for particle physics provide highly tolerant chips although dose and rate effects are not fully understood.

Electronics on III-V semiconductor materials, including optical components, are also usually hard to high levels. In part, this is because the materials are not usually such perfect crystals as silicon but devices such as MESFETs are not too sensitive to the details of bulk imperfections, so some damage is tolerable. In optical devices, such as semiconductor lasers, the very small active volume of modern components protects against big changes in performance.

Junction FETs are also relatively hard against ionising damage. These are often interesting for input devices of amplifying circuits because of potentially very low noise, since carrier conduction is not close to the interface as in MOS devices, but usually where long time constants can be used. However JFETs are not available in modern commercial integrated circuit technologies, where CMOS dominates; three quarters of the world market is for CMOS products [5].

Not all processes are suitable for every application. CMOS is most commonly used for low-power circuits and essential for logic design. A few hardened technologies are available and have been intensively investigated. Military applications have declined in importance in recent years and, in consequence, few specially hardened processes exist and even fewer foundry services, typically expensive compared to standard processes. Some companies and technologies available are Harris (AVLSI-RA CMOS and UHF-1X bipolar), Honeywell (RICMOS and SOI CMOS), TEMIC (DMILL BiCMOS), Maxim (bipolar). However, almost none of them are formally qualified to multi-Mrad levels, where export regulations can bring problems.

Because of the decline of military markets, there has been a big change of focus for commercial manufacturers who now look to space applications as one of the growth areas. However, foundry investments are now so huge (~$2 billion for state-of-the-art modern facilities) that only the largest markets justify such investments. In addition, some markets, such as for memory, are highly competitive with modest profit margins, so emphasis is on high-volume production with long-term contracts, and careful scheduling so the foundries are never idle. Particle physics, and other areas of science, do not come close to high volume. The largest LHC project requirements are equivalent to only a few days production for a single manufacturer.

Deep sub-micron technologies

Despite the small volumes of particle physics circuits, there is motivation to attempt to follow commercial trends (cost). The semiconductor industry continues to deliver larger chips at lower prices and to prevent this trend from declining, although it becomes ever more difficult. The well-

known "Moore's law" predicts that minimum feature sizes should halve every 6 years and the low cost of consumer products is evidence of the industry's success.

Standard commercial CMOS processes now use feature sizes well below 0.5µm, with 0.25µm and 0.18µm processes in large-scale operation. Wafer costs increase with time only slightly despite their larger area; 200mm diameter is the present norm, so even large chips are produced at lower price, once development costs have been amortised. As the feature size decreases, so does the gate oxide thickness. This is associated with lower voltage operation, reducing power, but it has had another important consequence, which is improved immunity to radiation damage.

It was well-known that immunity to oxide damage increases rapidly with decreasing oxide thickness, roughly as the square of the thickness. However, very thin gate oxides typical of deep sub-micron processes perform even better than this scaling would predict and have very high intrinsic hardness, apparently due to hole tunnelling from the oxide which reduces radiation induced trapped charge[6]. Combined with design techniques which protect against inter-device leakage, this has been shown to allow radiation tolerance in the multi-Mrad range [7] (figs. 2 & 3).

There are some major benefits of this approach, compared to using conventional hardened technologies: significantly lower price wafers, higher circuit density, state-of-the-art processing, and thus high yield and quality. There are also some risks: circuits must be user qualified, possible increased SEU sensitivity, and complications from the fact that very large companies with modern foundries and high-volume production do not encourage small customers.

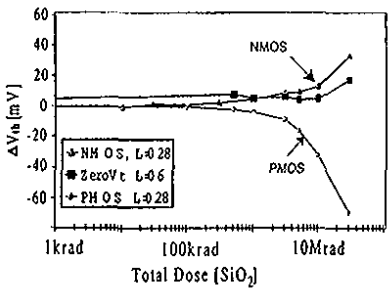

Fig. 2. Threshold voltage shifts measured on 0.25µm transistors [7].

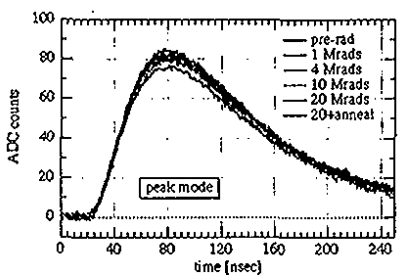

Fig. 3. APV25, for the CMS tracker, pulse shapes before and after irradiation [8].

5. Optical links in LHC experiments

Fibre optic links are attractive compared to electrical transmission because of low mass, absence of electrical interference, and high bandwidth, in most cases using less power. The distributed nature of LHC electronic systems means the technology is essential for some sub-detectors. R&D in the last few years with industry has begun to deliver components matching particle physics applications.

Optoelectronics is a fast moving area driven by telecommunications, local area networks (digital0 and cable TV transmission (analogue). However, particle physics requirements on material, power and cost targets are all lower than most commercial components offer, with the additional need for radiation tolerance. For short distance particle physics applications, the major cost drivers are transmitters and optical connectors.

There are several applications: the LHC machine clock and triggers, as well as control commands, will be distributed using a dedicated system used by all experiments, then custom systems matching the front-end electronics for digital control distribution at ~40Ms/s, high-speed digital data transmission at ~1Gb/s and analogue data transmission at 40Ms/s.

Fibres are not individually as robust as electrical cables, but optical fibre-ribbon cables with reinforced protective sheaths can be used, although customisation, e.g., to avoid magnetic material, has been required. For short links (~100m) used for particle physics, signal attenuation is not a problem, unless fibre or connector radiation damage were to be large, and this has been measured. At the telecommunications wavelength of 1.3µm, used for the CMS tracker analogue data transmission, standard single-mode fibre will be adequate, and digital requirements at all wavelengths are of less concern.

A number of different transmitters have been investigated for LHC, including various optical modulators, where light output can be varied by electrical signals. However, most progress has been made using components closer to the commercial mainstream.

Light Emitting Diodes are not suitable for analogue data transmission due to their non-linearity but appeared possible for digital links. However LED degradation is significant in high-radiation regions. Meanwhile, semiconductor laser diodes began to become available in larger quantities offering many features required: small size, compact packages (in some cases, with custom developments), low power, and good radiation resistance.

5.1 Semiconductor lasers

Semiconductor lasers are based on p-n diodes in a direct band-gap material, under forward bias to create the population inversion necessary for laser action. Wavelength depends on band-gap and is defined using compound semiconductors, e.g., InGaAs, to match the low attenuation transmission windows in optical fibres at 1.3µm and 1.5µm. Laser operation requires an optical cavity which is constructed in the Fabry-Perot laser by cleaving the crystal to create optical facets to act as partially reflective mirrors. Vertical Cavity Surface Emitting Lasers (VCSELs) emit, at ~850nm, transverse to the wafer surface, with the cavity constructed epitaxially by multiple dielectric interfaces.

A minimum current is required for laser action since photons are lost from the cavity by external emission and internal absorption. Values as low as a few mA and forward voltage drops of 1-2V are now available with output power of many mW. Above threshold, light output power is usually highly linear with current in edge emitting devices making them suitable for analogue transmission with 8-9 bit ranges such as the CMS tracker; fig. 4 shows a typical laser characteristic.

During irradiation, traps are created in the laser material which act as non-radiative recombination centres and reduce optical gain. However, modern heterostructure (i.e., engineered multi-element materials, such as InGaAsP) quantum well lasers naturally have small active volumes to minimise electrical power and maximise efficiency. Irradiation results on most lasers are extremely good.

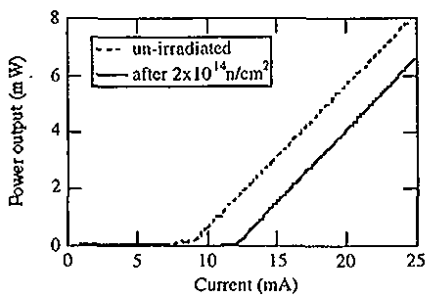

Fig. 4. Edge emitting laser characteristic before and after irradiation [9].

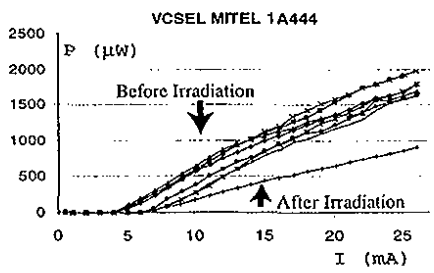

Fig. 5. VCSEL characteristics measured before and after irradiation with $3x10^{15}$ n.cm^{-2} [10].

Low cost is achieved in semiconductor manufacturing by high volume production with large numbers of die per wafer. Although optoelectronic wafers are smaller, so are die, and the same methods apply. Automatic testing before dicing maximises yield at the packaging stage, which is essential for cheap consumer products. Edge emitting lasers do not match this requirement, which is one barrier to increased use of optoelectronic technologies. VCSELs avoid cleaving before test, which reduces costs, and explains much of the interest in them. They do not at present have the linearity which would make them suitable for many analogue applications. This may change, but in any case most applications are digital.

5.2 Packaging

Packaging, where the emitter is accurately aligned to the core of an optical fibre, is an important cost driver and developments have been required to meet the requirements for LHC. Usually in experiments space is at a premium whereas commercial applications are often more concerned about robustness and the ability to exchange a single component without delicate handling. Single mode fibre is used for commercial long-distance links, and thus less expensive than multi-mode types, but multi-mode connectors require less precision because of the larger fibre core diameter and thus are cheaper than mono-mode connectors. This is another potential benefit of VCSELs.

Receiver diodes are commercial parts constructed using material matched to operating wavelength. Only for diodes located inside the detectors is radiation damage a concern; at 1300nm III-V materials are used and low bit error rates are demonstrated, while at 850nm silicon diodes can act as photodetectors, probably with adequate radiation tolerance.

5.3 High-speed digital links

For digital links, data should be transmitted with the ability to confirm data quality for asynchronous transmission. For systems like LHC where a well-defined clock is available everywhere, some savings in complexity can, in principle, be achieved by reducing error correction overheads. However, loss of synchronisation between transmitter and receiver caused, for example, by SEU errors could then cause severe problems of data corruption.

Commercial links which include error detection encoding and decoding electronics have been evaluated for ATLAS and CMS and some custom developments are under way. For the CMS ECAL, a GaAs CHFET serialiser is being developed to be coupled to a VCSEL transmitter while in CERN, a 0.25μm CMOS serialiser has worked impressively with commercial transmitters and could form the basis for several LHC applications.

Technology trends and constraints

From work in the last few years, some trends can be discerned.

6.1 Industrial developments

Many developments are dependent on co-operation with industry, with companies who are very large compared to those traditionally involved in sensor or mechanical engineering projects. Entry costs for electronic technologies are usually very high and commercial interest is frequently small for customers with distant projects and modest final orders. Some manufacturers were initially attracted by potential large LHC purchases but many quickly realised that particle physics projects were demanding and unconventional, perhaps offering little profit.

Nevertheless, access to modern technologies has been achieved, sometimes based on individual contacts, some of which have been enhanced by the opportunity to carry out funded R&D for future projects. However, the risk of dependence on a single vendor can be increased, and commercial strategies and technologies do sometimes change at very short notice.

6.2 Custom circuits

Development of complex ASICs is a long-term task, typically requiring ~1year/cycle of design, fabricating and testing, with 4-5 iterations/circuit before finalisation. This must be complemented by much evaluation to a detailed level close to operational conditions, and radiation qualification, so has turned out to be a very long term enterprise [1,11]. Testing,

meaning much more than mere demonstration of functionality, is often a weak point in circuit development [12]. In most detectors the electronic readout systems, including control logic, are technically much more complex than sensors in which, in contrast, there are often heavier investments.

Developments are expensive, with typical ASIC foundry costs of ~$150K for a few wafer engineering runs, but usually to reach this point some expectation of sizeable future orders is needed. Most particle physics projects could be satisfied by a small number of wafers so, in purely commercial terms, ASIC development is unjustified and this trend is increasing. Multi-project runs have been utilised successfully but are not usually a service offered by foundries. Small projects are dependent on sharing costs and time-scales with larger projects, which may not always be feasible.

The trend to finer feature sizes will continue to increase entry costs and technical difficulties, as each new technology must be characterised for analogue performance. Although digital circuits dominate, front-end amplifiers and filters are essential and critical components, whose success is intimately linked to the overall circuit design.

Given the large scale and investments in these projects, it seems important to eliminate competition early, building multi-group teams, and gradually evolving new designs from proven ones where possible.

Programmable logic

FPGA developments have been rapid in recent years and rely heavily on the success of the integrated circuit industry. In contrast to ASICs, they offer flexibility and programmability, based on standard components. Costs are falling, size is growing and power is being contained [13]. As with IC technology in general, this trend will be difficult to maintain but it seems assured for some years to come. In systems where space and radiation constraints do not dominate, they are already heavily used.

Optical technologies

This is perhaps the fastest changing area, where most new developments for the future may be expected. Activity in fibre optic links, which is subject to many of the same constraints as ASICs, continues to grow. There is continuous development of other optoelectronic components to provide new functions, like optical switches or holographic memories, which promise eventually to revolutionise some particle physics systems.

6.5 Tools

Design tools are essential to undertake circuit developments; they are usually expensive but collaborative ways have been found to make them accessible to a large community. However, modern circuits also require fast, high-speed, and expensive test instruments, which can only be purchased by some large laboratories and need qualified professionals to support. Some labs carry out testing of analogue circuits which often require greater flexibility and customisation closer to the end use. Both aspects are important for success.

Conclusions

The opportunity to be innovative in the R&D stage stimulated some immature, or even unproven, technologies. Ambitious use of novel technologies is not new to particle physics but the scale of the LHC experiments, and possible future projects, introduces a new factor, which is the discipline of industrial scale production and assembly. In electronics, this discipline is already widely felt in the development stage.

There is still some way to go before LHC switch-on and there is much important work to be done which was not covered here on electronic-related issues like power supplies, assembly, services and other practical issues which must be completed to ensure successful long-term operation at LHC.

The SSC and CERN Detector Research and Development programmes were very beneficial in evaluating potential technologies and hastening progress.

References

[1] G. Hall *LHC front end electronics.* Paper presented at INSTR99, IC/HEP/99-9 http://www.hep.ph.ic.ac.uk/preprints.html

[2] Proc. LHC Electronics _Board Workshop. CERN Report CERN 99-09(1999) http://hep.physics.wisc.edu/LEB99/

[3] Proc. LHC Electronics _Board Workshop. CERN Report CERN 98-36 (1998)

[4] Proc. LHC Electronics _Board Workshop. CERN Report CERN 97-60 (1997)

[5] *The National Technology Roadmap for Semiconductors.* Semiconductor Industry Association. (1997). http://www.semichips.org/

[6] N.S. Saks et al., IEEE Trans. Nucl. Sci., NS-31 (1984) 1249

[7] P. Jarron & A. Marchioro. Ref [4], 139.
RD49 Status Report CERN/LHCC 2000-003 (2000)
http://www.cern.ch/RD49/Welcome.html

[8] http://www.te.rl.ac.uk/med/apv25_web/apv25_top.html
http://pcvlsi5.cern.ch:80/CMSTControl/documents/Marcus/APV25_Dec99.pdf

[9] K. Gill et al. Ref [4], 277.

[10] D. Charlton et al. Ref [2], 185.

[11] A. Lankford, *Developing and Commissioning Babar Electronics,* Ref. [2], 41

[12] J. Christiansen, *Testing LHC Electronics,* Ref. [2], 41

[13] P. Alfke *The future of Field Programmable Gate Arrays,* Ref. [2], 36.

TIME-OF-PROPAGATION COUNTER — A NEW CHERENKOV RING IMAGING DETECTOR —

Takayoshi Ohshima*
Physics Department, Nagoya University
Chikusa, Furo, Nagoya 464-8602, Japan

ABSTRACT

A new particle identification detector based on measurements of both Time-of-Propagation (TOP) and horizontal emission angle (Φ) of Cherenkov photons is proposed here. Some R&D results are also reported.

1 Introduction

Measuring of the Cherenkov angle (θ_C) is currently one of the most promising ways to identify high-energy charged particles. Depending on the particle, its momentum range, and experimental condition, there are various ways to do this using liquid, gas, or solid radiators with gas chambers or photo-multiplier tubes (PMT) as photon detectors. The Cherenkov ring image can be created using the proximity focussing, focussing mirrors, or pin hole projection, such as in RICH[1] and DIRC[2] type of devices. We propose here a new approach to the DIRC method, by measuring the ring image detecting both Time-Of-Propagation (TOP) of Cherenkov photons in the quartz radiator bar and horizontal emission angle (Φ) at the bar-end. This is in contrast to the BaBar DIRC, which measures the x and y coordinates.

In order to further improve the particle identification (PID) ability of the KEKB-BELLE spectrometer[3], in particular the K/π separation, the new detector should be compact in radial direction. The first attempt to propose a compact DIRC detector was a focussing counter, proposed by Kamae et al.[4]. It would eliminate a large projection volume, such as in the BABAR DIRC[2]. A small, vertically focussing mirror was proposed to reduce the vertical aberration. However, the horizontal aberration still remained, thereby weakening the PID ability of such a device, especially in the case of inclined incident particles. The proposed TOP counter, which uses the horizontal focussing, renders both of these aberrations effectively harmless. In addition, it can be made compact, and deliver the good particle separation.

To aid the readers in visualizing the principle of TOP counter, Fig. 1 illustrates the internaly reflecting Cherenkov photons propagating in a rectangular quartz bar: (a) top view and (b) side view. TOP is inversely proportional to the z-component of the light velocity: TOP(ns) = 4.90 $\times L$(m) / q_z, where q_z is the z-component of unit velocity vector and L is the propagation length along z direction. Let's briefly evaluate separation ability using this method. For example, the TOP difference between 4 GeV/c K and π is about 100 ps or larger for L = 2 m. Therefore, a

*Author's e-mail: ohshima@hepl.phys.nagoya-u.ac.jp, tel: +81-52-789-2447, telefax: +81-52-782-5752.

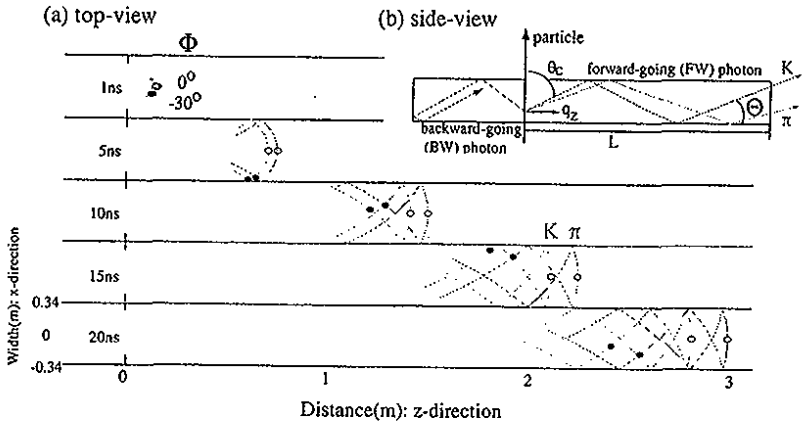

Figure 1: Illustration of PID principle of TOP counter. Parts of Cherenkov ring image, produced by a charged K and π with a normal incident onto this plane, are shown as propagating in a quartz-bar in (a). The quartz-bar has a rectangle cross section, width of which is set to 0.68 m for an illustration purpose, and its refractive index is $n = 1.47$. The elapsed time in ns is shown at the left-hand side. Curves (every 1° step in Φ) are the Cherenkov rings for π and K, respectively, and open and closed circles indicate photons emitted at $\Phi \simeq 0°$ and $-30°$. A side view of propagating photons is illustrated in (b). The photo-multipliers are placed in such a way as to detect the reflected photons (BW) toward the detectors (see also Figure 2). TOP is inversely proportional to the z-component of unit velocity vector (q_z).

time measurement with $\sigma = 100$ ps for a single photon yields 1 σ separation, and accordingly the total separation gives approximately a square-root of detectable number of photons (N_{ph}) times σ. That is, forward-going (FW) detectable photons is $N_{ph} \approx 30$ for a normal incident particle to 20 mm-thick quartz radiator, and its separation is expected to be 5.5 σ. When the backward-going (BW) photons are also detected as illustrated in Fig.1(b) by reflecting at an opposite end, the separation could be enhanced further by a factor of $\sqrt{2}$.

The TOP counter is a Time-Of-Flight counter, which detects the Cherenkov photons rather than the scintillation photons. Two substantial and undesirable effects of the precise TOF counters with the plastic scintillators can be eliminated: 1) While a decay-constant of fast counting scintillator is typically ~2 ns, the Cherenkov radiation does not have a decay mechanism, so no corresponding effect exists. 2) While the propagation paths of scintillation photons to a certain horizontal emission angle Φ, (see Fig. 1(a)) are not unique due to their uniform emission over 4π solid angle, they are unique for the Cherenkov radiation photons. Because of this, the Cherenkov photons could provide a comparable or even higher time resolution than the TOF scintillation counter, in spite of having fewer radiated photons. The Cherenkov Correlated Timing detector [5] is similar to the TOP counter, but without the Φ angle segmentation.

In order to evaluate the achievable K/π separability of the TOP counter, we optimize its parameters as illustrated in Fig. 2, where the butterfly-shaped horizontal focussing mirror with an arc radius of 250 mm is designed to have the

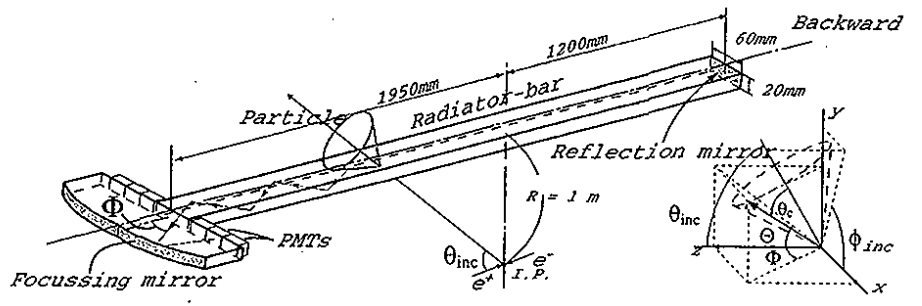

Figure 2: Structure of the TOP counter. Basic parameters are indicated in the figure. Anode array of PMTs is arranged on the focal line of the butterfly-shaped focussing mirrors along to x direction. Since KEKB is an asymmetric collider, the quartz-bar is accordingly configured as z-asymmetric relative to the interaction point (IP).

Φ-aparture of ±45° and dispersion of $d\Phi/dx = 0.5°/1$ mm. Root-mean-square of the focussed accuracy is $\Delta x \approx \pm$ 0.4 mm. The radiator-bar has a length of 3150 mm, width of 60 mm and thickness of 20 mm, and its backward-end surface has a reflecting mirror. The bar and focussing mirrors are made out of synthetic optical quartz with refractive index (n) of 1.47 at wavelength of $\lambda = 390$ nm. These counters would be placed at 1 m radially away from the interaction point of the KEKB-BELLE detector to form a cylindrical structure as the barrel PID counter.

The differences of TOP and TOF (measured from IP to the TOP counter) between K and π have the same sign under most conditions, and therefore adding both TOF and TOP could improve the separation; therefore, TOP is hereafter defined as a sum of TOP and TOF, unless otherwise specified.

2 Expected Separability

There are three dominant contributions which limit the best possible K/π separability:

(1) chromatic effect of the Cherenkov photons,

(2) aberration effect of the focussing mirror, and

(3) transit time spread (TTS) of the photomultiplier tube (PMT).

Figure 3 shows TOP errors from the above three contributions, and the K/π TOP and TOP+TOF time differences, δ(TOP) and δ(TOP + TOF), for two examples representing the BELLE experimental conditions (see also Ref.[6], which discusses other cases). Since both contributions,(1) and (2), rise steeply at large Φ, Φ acceptance is limited to $|\ \Phi\ | < 45°$. Adding the error in the TTS, $\sigma_{TTS} = 80$ ps, which will be discussed later, and other contributions, such as the start-signal uncertainty of 25 ps, results in a total uncertainty of 84 ps for error (3). When a particle's incident polar angle θ_{inc} gets smaller than 40°, δ(TOP) reverses its sign compared to the TOF difference (see Fig. 3(b)), and the separation power decreases somewhat.

The expected detectable number of FW photons is approximately 35 and 115, for examples shown in Fig. 3(a) and 3(b), respectively, assuming the PMT's quantum efficiency (QE) of ≈25%. When the particle hits the TOP counter at $\theta_{inc} \sim 90°$, it also exits a sufficient number of BW photons. They reach PMT's 15-20 ns later compared

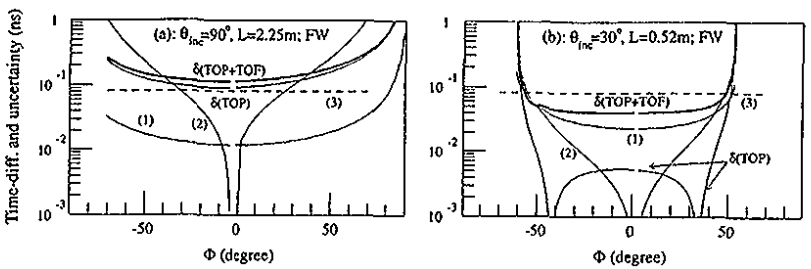

Figure 3: Three dominant contributions to time measurement error, (1), (2) and (3), as discussed in text, and TOP differences for 4 GeV/c K and π. TOP counter (see Fig.2) is configured to form a cylindrical shape and operates at B=1.5 T in KEKB-BELLE. $\theta_{\rm inc}$ is the polar angle of an emitted particle from IP (see Fig.2). In these figures, only FW photons are taken into consideration. In (b) δ(TOP) has negative sign at $|\Phi| < 40°$. Due to the magnetic field effect, the incident particle to the TOP counter is bent in the azimuthal direction and therefore the *contributions are not symmetric, as seen in figures.*

to FW photons, and therefore the detection and the identification of both FW and BW photons is relatively easy. When the particle hits the TOP counter at $\theta_{\rm inc} > 90°$, the BW photons play the leading role.

Before examining the expected separability, we would like to bring attention to some specific aspects of the TOP counter.

- The time spread of Cherenkov radiation along the particle trajectory over the thickness of quartz bar is compensated by the corresponding variation of photon propagation time. The maximum variation of the sum of these times, which is $\sigma \sim$20 ps, occurs at the normal incidence, and it is less than 20 ps at any other incident angle. This effect is much smaller than PMT's TTS, and therefore the vertical aberration is negligible for the TOP measurement.
- Figure 4(a) and 4(b) show (TOP+TOF) distributions as a function of Φ for the horizontal focussing, and as a function of the vertical emission angle Θ for the vertical focussing, respectively. In the former case, the photons distribute rather uniformly over the angle, and also the slope ∂(TOP + TOF)/∂(angle) is rather smaller compared to the second case.. Therefore the horizontal focussing was chosen to achieve a better resolution and also easier detection.
- The contribution from the multiple scattering (MS) is also small: $\Delta\theta^{rms}_{\rm space}(MS)$ is 2.9, 1.5, 0.98, and 0.74 mrad, while the difference of K/π Cherenkov angles $\Delta\theta_{{\rm C};K/\pi}$ is 104, 25.9, 11.6, and 6.5 mrad for a normal incident 1, 2, 3, and 4 GeV/c particle, respectively.
- The BELLE-CDC (Central Drift Chamber) provides precise enough information, regarding the particle incident position, angle and momentum, to nullify their effects on the TOP measurement. The z-position resolution is about 2 mm, which corresponds to a time uncertainty of about 10 ps. Ambiguity of momentum measurement leads to an uncertainty of the Cherenkov emission angle, as $\sigma_{\theta_C} = \left(\frac{\cot\theta_C}{\gamma^2}\right) \cdot \left(\frac{\sigma_p}{p}\right)$: This uncertainty is much smaller than $\Delta\theta_{{\rm C};K/\pi}$ even at $\sigma_{\rm P}/{\rm p} = 1$ %. The error in the particle's incident angle $\theta_{\rm inc}$, contributes less than 10 ps in error of the TOP measurement , in the case of BELLE, because $\phi_{\rm inc}$ error does not intrinsically affect TOP since $\frac{\partial t_R}{\partial \phi_{\rm inc}}|_{\theta_{\rm inc}} = 0$.

Taking into account all contributions mentioned above, a simulation study assumed to measure only the eariest arrival photon at individual anodes, and assuming that PMTs have $\sigma_{\rm TTS} = 80$ ps and anode width of 1 mm. A *reference (TOP vs Φ)- distributions are obtained for* Cherenkov photons generated at the middle of quartz thickness, with n = 1.47 and by K and π particles.

Figure 4 shows results of these simulations (open circles and crosses), including the reference distributions (curves). Figure 5 shows the Log-Likelihood distribution, includeing the reference. The resulting separability is $\mathcal{S}(= \sqrt{2\Delta ln\mathcal{L}}) = 5.7$ for 4 GeV/c K/π at $\theta_{\rm inc} = 90°$. Figure 6 shows the calculated separabilities of the TOP counter for the BELLE configuration. Figure 6 also shows the separability for π's in $B \to \pi\pi$ decay (a thick curve), *which represents the highest momentum limit at the BELLE* experiment. It is found that $\mathcal{S} > 5$ could be achieved at any barrel region of $\theta_{\rm inc} = 30° - 130°$.

3 Multi-anode PMTs

We are performing R&D on two kinds of PMTs for the TOP counter. The photon detector should have the following properties:

- Single photon sensitivity,
- High time resolution, for example, $\sigma_{\rm TTS} \lesssim 100$ ps,
- Position sensitivity, for example, $\sigma_x < 0.5$ mm,
- Operability under magnetic field of 1.5 T at BELLE.

The first three items are well realized by a commercially available PMT: Hamamatsu R5900U-00-L16. Our R&D work on the TOP counter is proceeding with this PMT, as reported below. L16 is a linear-array 16-anode PMT with 0.8×16 mm^2 anodes of 30×30 mm^2 size and 1 mm pitch. It has a gain of 2×10^6 at a supply voltage of 800 V over 10 dynodes, and gives a 0.6 ns risetime. We adjusted the HV divider to supply higher voltage to the first two dynodes, compared to a standard design, in order to reach the time resolution of σ <100 ps. Figure 7 shows the measured time resolutions in the single photon mode, as a function of (a) the ADC pulse-height using all 16 channels of the L16 PMT, and (b) the anode number withing the L16 PMT (about 75 ps was obtained on average). The data were obtained using a 400 nm light pulser, and with a 1 mm-wide slit in front of the PMT. Without the slit, cross-talk was observed, especially under a high multi-photon irradiation, which also affected the resolution. Its study is being carried out now.

Since L16 cannot operate in a large magnetic field, we have been examining other possibility, such as the fine-mesh multi-anode PMTs: Hamamatsu R6135MOD-L24 (square shaped of area 39×39 mm^2) and L24X (round shaped). *L24 has 24 anodes of size 0.8×26.5 mm^2, and pitch of 1.1 mm. While L24* has a 2.5 mm distance between the photocathode and the first dynode, L24X has 1 mm distance, but keeping other essential parameters the same. With 24 dynodes, a gain of $2(8)\times10^7$ is achieved at 1500 (2000) volts for L24 (L24X). With no magnetic field, the position resolution is only about 2 mm, however, for field higher than 0.2 T, it improves to σ <0.5 mm, as seen in Fig. 8(a). The fine-mesh type PMT does not yield a peak in the single photon distribution spectrum, but instead a continuous distribution without a deep valley between signal and noise, as indicated in Fig. 8(b). Time resolution is measured, for L24X, by varying the magnetic field strength under which the maximum allowed high-voltages are applied. This data are plotted in Fig. 8(c) as a function of gain relative to that with no magnetic field. The PMT's gain reduces quickly with the magnetic field and time resolution also gets worse. To date we have reached $\sigma \sim$120 ps at B <0.6 T.

4 Beam Test

In order to confirm the essential and expected characteristics of the TOP counter, beam tests were performed at KEK-PS using π beam. A test counter was constructed with the structure as described in Fig. 2, but the quartz bar length was 1 m and an absorptive filter instead of the reflection mirror for BW photons at the bar end was prepared. Six L16 PMTs were attached to the focussing mirrors and accordingly, 96 anode signals in total were read out. Overall detection efficiency of photons, which come to the focal line surface, not including the PMT's QE, was nearly 20% at current configuration: Photoelectron detection efficiency of the L16 PMT was about 1/2, and an effective coverage by L16 sensitive area over the mirror surface was about 40%. The above PMT's insensitive area, most of which was due to the mechanical structure, would reflect back the photons and such photons hit wrong anodes after being reflected by the aluminum coated focussing mirror (we will call such photons the mirror-reflected photons). In order to avoid this unwanted phenomena, the absorptive filters were inserted in front of such L16 dead surfaces. The time resolution and the mirror-reflected photon distribution were measured by injecting single photons from the light pulser through an upper side of the focussing mirror or the quartz bar.

The beam was tuned to hit the TOP counter at L = 0.02 m nominally. The recorded data are shown in Fig. 9, where a single photon peak is clearly seen in the ADC spectrum, which coincides with the spectrum produced by light-pulser single photons. Figure 9(c) shows a timewalk-corrected TDC distribution where two small contributions, besides Cherenkov signal photons, can be found: Cherenkov photons produced by the knock-on electrons, and the mirror-reflected photons. The resulting time resolutions, taking into account all 96 anodes, were about σ = 85 ps, as plotted in Fig. 10. These results are consistent with those observed with the light pulser. The chromatic contribution is insignificant at this configuration, and the L16 PMT's TTS dominates the resolution.

Next, the beam position was moved to L = 1 m, and the beam momentum was set to 1.1, 2, and 4 GeV/c. The expected number of anodes, which fired, was 6, and we observed an average 6.3, at each momentum set. We applied a time cut to reject the contributions from the knock-on electrons and the mirror-reflected photons. Figure 11 shows the observed Cherenkov ring image as a function of Φ angle. Because of longer propagation length in this case, the TDC distribution produced by the knock-on electrons are widely spread. We did not have a beam tracking chamber system, and therefore the beam divergence, as defined by trigger scintillation counters, was not as precise as expected for the BELLE spectrometer, where its contribution is expected to be negligable. Therefore, a simple but tricky analysis was carried out. Triggered samples are required to have a signal in the certain anode. For example, for a case of the 27th anode, a cut within the first 150 ps time duration of its measured raw time distribution of 350 ps (FWHM), would restrict the beam divergence somewhat. Measured resolutions for some anodes are plotted in Fig. 10; a fairly good agreement with the expectation can be seen, allthough one must say that the errors are large. The parabolic rise of the calculated resolution at large Φ is due to the aberration effect of the mirror rather than the chromatic contribution.

5 Discussion and Summary

The TOP counter is compact and has a high particle separability. Due to the horizontal focussing and thin radiator thickness, the size of a quartz bar cross section can be disregarded, and therefore it does not need a large standoff projection space such as with the BaBar DIRC. In order to make this TOP counter feasible, we still need more R&D work.

First, confirmation of basic TOP behavior, especially the performance at L = 1 m or longer distances, and using a tracking chamber during the next beam test.

Second, increasing the detected number of photons is the most important issue, and two approaches are being considered. One way is to employ light-guides between the mirror and the PMTs. Other way is to develop a PMT with larger sensitive area and large number of anodes. Such detector could be utilized, for example, in the fixed target experiment operating with no magnetic field.

To utilize the TOP counter as the next BELLE PID detector, one has to develop a L24 type of PMT, or its equivalent capable of detecting single photons in a large magnetic field of 1.5 T, with position sensitivity of σ_x <0.5 mm and TTS of σ_{TTS} <100 ps. R&D work to develop a L24 type of PMT is under way.

Remarks:

- Adding TOF to TOP helps PID mainly for a low momentum particle. However, for a very long flight-path length, which is possible at some fixed target experiments, one obtains a sufficient separability, as indicated in Table 1, while $\Delta\theta_{C;K/\pi}$ produces only a small TOP difference. Further enhancement of separability can be achieved by improving the PMT's TTS, and/or increasing the detected number of photons. The TOP counter acts in this case as a kind of high resolution TOF counter by means of Cherenkov radiation.

Flight length R(m)	Separability S			
	p = 4 GeV/c		p = 10 GeV/c	
	FW	BW	FW	BW
0	5.7	8.3	1.5	1.5
1	7.4	9.0	1.5	1.5
5	11.7	11.6	1.9	2.2
10	17.6	14.5	3.0	2.9

Table 1: Achievable separabilities with various flight path-length (R). The simulation results of our TOP detector, where FW and BW photons are separately detected, are listed for particles with θ_{inc} = 90° with no magnetic field. The differences of θ_C between π and K are 6.5 and 1.0 mrad for p = 4 and 10 GeV/c, respectively, and those of the TOF are 231 and 37 ps at R = 10 m.

- Photons propagate in a polished scintillator, keeping their original angle information. It may be interesting to use a scintillator instead of the quartz, although the situation is still not thoroughly understood without an additional investigation. The arrival time distribution of photons at individual Φ segments will spread because of its finite decay time constant and 4π emission. Owing to high TTS making up for a fewer number of photons per segment compared to an ordinary TOF counter, the overall achievable TOF resolution by multi-segment measurements could well be improved.

- Although the separability for particles of large incident angle $\theta_{inc} \leq 120°$ is rather low as seen in Fig. 6, it could be recovered by equipping an inclined reflection mirror, for instance, of 45°, at the backward end. It makes the reclining Cherenkov ring image stand up to the normal direction so as to propagate the full bar length with the best configuration for separation. While an opposite effect occurs for BW photons generated by a normal incident particle, a rather sufficient TOP difference is already produced by propagating a certain long distance before the photons arrive at the reflection mirror. Optimization of the inclining angle should be investigated.
- The present design of the focussing mirror has a horizontally extended structure that does not seem suitable as a barrel detector. A simple and practical solution is to tilt the counter around the z-axis.

Acknowledgements

I greatly appreciate Mr.Kozaburo Fujimoto for his help to prepare this article in an electronic form. I also gratefully acknowledge Hamamatsu Photonics K. K. for their sincere cooperation to develop L16 and L24 PMTs. This work is supported by Grant-in-Aid for Scientific Research on Priority Area (Physics of CP violation) from the Ministry of Education, Science, and Culture of Japan. The R&D tasks have been carried out by the members of TOP group: M. Akatsu, Y. Enari, K. Fujimoto, Y. Higashino, M. Hirose, T. Hokuue, K. Inami, A. Ishikawa, S. Matsui, T. Matsumoto, K. Misono, T. Ohshima, A. Sugi, A. Sugiyama, S. Suzuki (Nagoya U.), H. Okuno (KEK) and A. Yamaguchi (Tohoku U.).

References

[1] For instance, see, J. Va'vra in Proceedings of 7th Int. Conf. on Instr. for Colliding Beam Physics, INSTR99, Hamamatsu, Japan, November 15-19, 1999.

[2] B. Ratcliff in Proceedings of 7th Int. Conf. on Instr. for Colliding Beam Physics, INSTR99, Hamamatsu, Japan, November 15-19, 1999.

[3] For the description on KEK-B factory and BELLE detector, for instance, see J. Haba, Nucl. Instr. and Methods, A368 (1995) 74; T. Nozaki, Nucl. Phys. B(Proc. Suppl.) 50 (1996) 288.

[4] T. Kamae et al., Nucl. Instr. and Methods A382 (1996) 430.

[5] K. Honscheid, M. Selen and M. Sivertz, Nucl. Instr. and Methods, A343 (1994) 306; H. Kichimi, Nucl. Instr. and Methods, A371 (1996) 87; idib. A371 (1996) 91.

[6] M. Akatsu, M. Aoki, K. Fujimoto, Y. Higashino, M. Hirose, K. Inami, A. Ishikawa, T. Matsumoto, K. Misono, I. Nagai, T. Ohshima, A. Sugi, A. Sugiyama, S. Suzuki, M. Tomoto, and H. Okuno (KEK, Tsukuba), Nucl. Instr. and Methods, A440 (2000) 124-135.

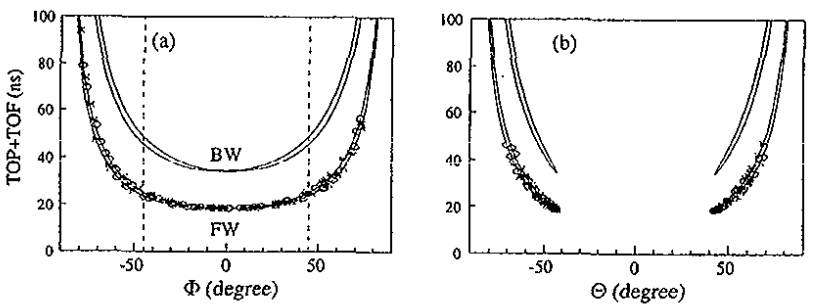

Figure 4: TOP+TOF distributions using (a) horizontal and (b) vertical focussing cases for 4 GeV/c normal incident particle. Because of a tilt in the azimuthal angle of the incident particle due to a magnetic field, two inclined, but symmetric, ring images are formed by FW and BW photons in both cases. Open circles and crosses indicate FW photons generated by π and K particles, respectively, in a simulation study.

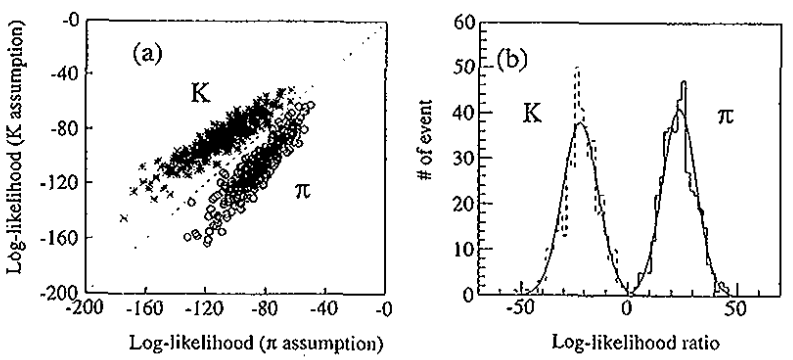

Figure 5: (a) Log-Likelihood distribution for 4 GeV/c K and π at $\theta_{inc} = 90°$. Horizontal and vertical axes indicate the Log-Likelihoods for π and K hypotheses, respectively, and open circles and crosses are the generated π and K samples. (b) The Log-Likelihood ratio distribution.

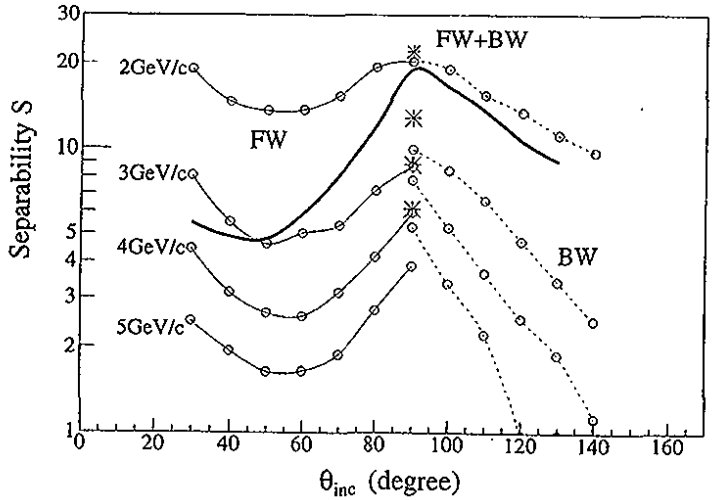

Figure 6: Expected K/π separability for the BELLE configuration. Thin curves are obtained by detecting either FW or BW photons, while crosses are obtained by detecting both photons at $\theta_{inc} = 90°$ case. Momenta of particles are indicated at the left-hand side. The thick curve represents the separability for the highest momentum π's at the BELLE experiment, coming from the decay of $B \to \pi\pi$.

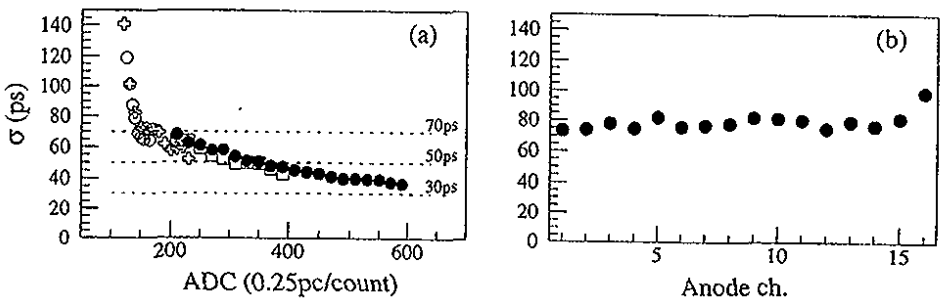

Figure 7: Time resolution of L16 PMT. (a) Time resolution σ vs ADC pulse-height. Measurements were performed four times by changing an intensity of a light pulser, as plotted by open and closed circles, square and crosses. Single photon pulse-height peak corresponds to about 170-th ADC channel. (b) Time resolutions for single photon are measured over all 16 anodes. For (a) and (b), a 1 mm-wide slit is placed in front of the PMT, and HV of 1000 V is applied.

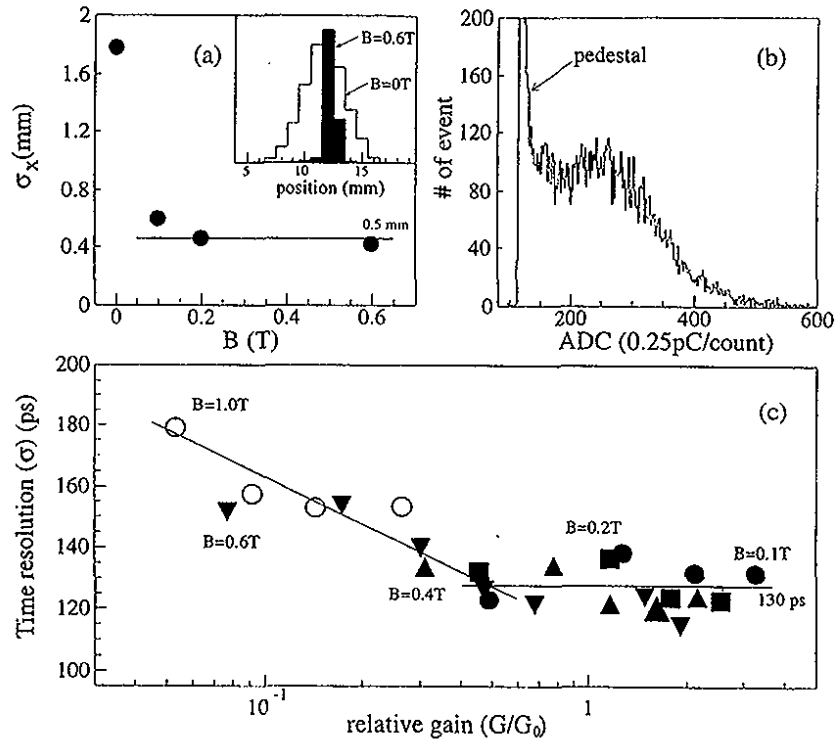

Figure 8: Perfomance of L24 and L24X PMTs. (a) Position resolution (L24) vs magnetic field. Subset is a spartial distributions with and without field. (b) Pulse-height distribution of L24X PMT. (c) Time resolution (σ) of L24X as a function of relative gain (G/G_0), where G_0 is the amplification gain with B = 0. Individual magnetic field strengths are indicated in the figure. The measurements were carried out using both a light pulser with a single photon emission and a 1 mm-wide slit in front of PMTs.

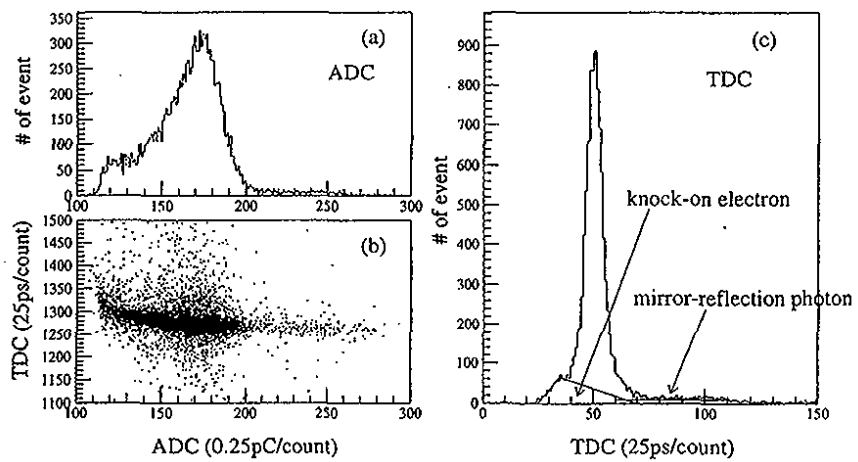

Figure 9: Data obtained in the beam test with L = 0.02 m. (a) ADC distribution, (b) ADC vs TDC scatter plot, and (c) Timewalk corrected TDC distribution. Resolution of σ =80 ps was obtained by subtracting a time uncertainty in the start signal. These data are obtained using the 20th anode, and in a 2 GeV/c π beam.

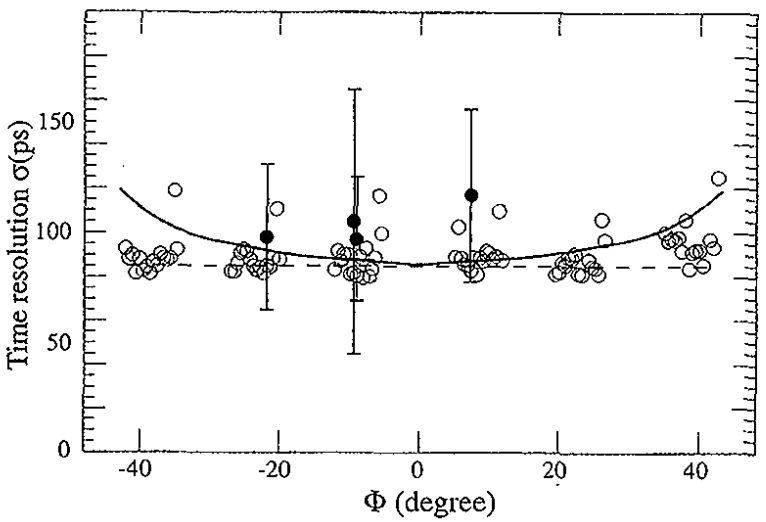

Figure 10: Measured time resolutions over 96 anodes at L = 0.02 m and 1 m for 2 GeV/c πs. Horizontal axis represents the readout anode channels in the form of the Φ angle. Open circles are the measured time resolutions measured at L = 0.02 m, and closed circles with error bars were obtained at L = 1 m by applying a particular analysis method mentioned in the text. The solid curve indicates a MC expectation at L = 1 m, based on the achieved resolution, and at L = 0.02 m, indicated by a dotted line.

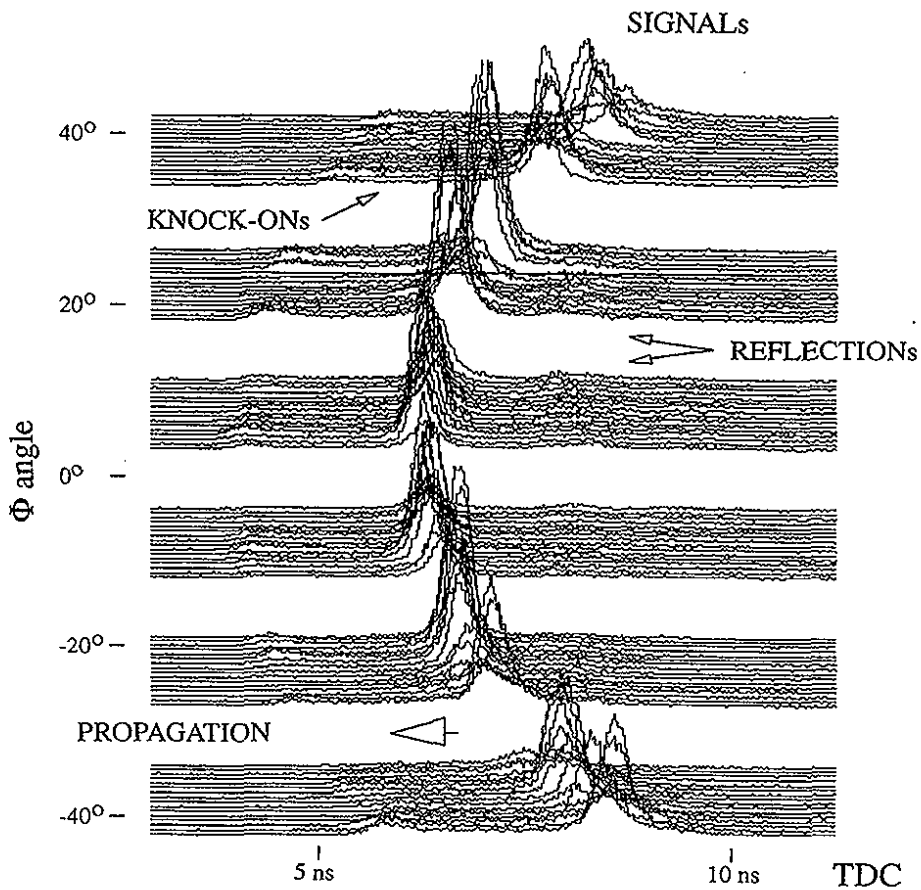

Figure 11: Cherenkov ring image formed by the FW photons, produced by a 4 GeV/c πs beam, perpendicular to the bar, and at L = 1 m. Timewalk is not corrected out.

MIPA: A NEW MICRO-PATTERN DETECTOR*

P. Rehak, G.C. Smith, J.B. Warren and B. Yu
Brookhaven National Laboratory, Upton, NY 11973, USA

ABSTRACT

An anode-cathode array is being developed for electron multiplication in gas that lends itself to easy fabrication with lithographic techniques. Comprising an assembly of anode pins that are recessed into a closely-packed hexagonal cathode, the MIcro-Pin Array (MIPA) represents a promising addition to micro-pattern detectors with two-dimensional sensitivity. We describe the electrostatic rationale behind the MIPA detector's design, the fabrication technique, and X-ray results that illustrate electrical stability and high rate capability.

1 Introduction

A novel electron amplifying micro-structure is being developed for use as a position sensitive X-ray detector for dynamic crystallography at the National Synchrotron Light Source (NSLS) at Brookhaven National Laboratory. The energy of the X-rays, about 10 keV, is within the energy region where several centimeters of xenon at atmospheric pressure are sufficient to fully absorb the scattered radiation. The detector should provide a high-resolution image of the diffraction patterns with an effective number of pixels of at least 1 million, with the same resolution in both x and y directions. This implies that the relative position resolution should be better than one part in a thousand in each direction. Furthermore, the total rate on the detector can approach 100 MHz.

The linear position resolution of the detector should be slightly smaller than the photon beam size, which is about 300 μm rms for current NSLS crystallography beam lines. It is very difficult to achieve these relative and absolute resolutions under such a high flux of incoming photons

*THIS RESEARCH WAS SUPPORTED BY THE U.S. DEPARTMENT OF ENERGY UNDER CONTRACT NO. DE-AC02-98CH10886.

using a global projective position encoding method, such as the standard wire chamber or MSGC technology.

However, the use of some form of "micro-pattern" gas amplification may be a suitable approach to achieve the required specifications, particularly if the complete detector is fabricated from smaller independent segments. In addition, the recently published method of decreasing parallax error[1] makes a xenon gas detector a suitable candidate for dynamic crystallography.

2 Stability of the Gas Amplification

To achieve the required longterm, stable performance under a high flux of radiation, the amplification region of a micro-pattern gas detector should at minimum satisfy the following two conditions:

1. No dielectric surface near the avalanche region.
2. First order stability of the field in the avalanche region with respect to electric discharge.

The importance of the first condition is well documented in the literature dealing with instabilities in most of the micro-pattern gas detectors[2], and is easy to understand. The charge on the surface of a dielectric depends on the previous history of the electric field and charges in the region above the surface. The presence of the charges on the surface influences the electric field in the amplification region leading to instabilities. Attempts to overcome this problem by using very high resistivity glasses or other layers have not been fully successful.[3]

The second condition concerns stability of gas amplification. In order to achieve the desirable gas gain in the amplification region, a set of suitable voltages are applied on the electrode structures of the gas detector. In the absence of any space charges within the gas of the detector, the geometry of the amplification region and the applied voltages define completely the electric field within the avalanche region. The amplification of the electrons in this region, filled with a particular gas mixture at a given pressure, depends only on the electric field. However, once the avalanche takes place, electrons are removed from this region much faster than the positive ions, modifying the electric field. If this modified electric field corresponds to one with higher gas gain, electrons arriving in the avalanche region produce even more charge and the combined effect can lead to a run-away phenomenon or an electric discharge. The condition of "first order stability" requires that the applied field in the charge free amplification region corresponds to a maximum of the gas gain. Any deviation from this field due to the presence of space charge should decrease the gas gain and prevent the amplification run-away.

Our analysis models the gas amplification according the classical work by Townsend. The avalanche process is described by the number of ionization collisions per unit length, called the first

Townsend coefficient, α. From this definition the natural logarithm of the gas gain is

$$\ln G = \int_{s_1}^{s_2} \alpha(U, U', s)\, ds, \tag{1}$$

where α can be a function of the voltage U and of the electric field $E = U'$ at a given point along the electron trajectory, s. s_1, and s_2 are the first and the last points on the trajectory of electrons within the avalanche region respectively. We will moreover assume that the potential at the first and the last point of this region are U_1 and U_2, respectively. The second requirement on the stability is thus reduced to a variational problem of finding a function $U(s)$ that maximizes the gas gain in Eq.1, with given values of voltages at both end points. ($U(s_1) = U_1$ and $U(s_2) = U_2$).

The first Townsend coefficient α does not depend explicitly on the integration variable s, and the Euler equation

$$\frac{\partial \alpha}{\partial U} - \frac{d}{ds}\frac{\partial \alpha}{\partial U'} = 0 \tag{2}$$

gives the trivial solution $U' = (U_2 - U_1)/(s_2 - s_1) = \text{const}$. This is the case of a uniform field in a parallel plate geometry. However, for the values of α for our geometry, the uniform field corresponds to the minimum rather than the maximum of the gain.

To obtain the function $U(s)$ that maximizes gain, the class of functions $U(s)$ in Eq.1 must be constrained to those satisfying the electrostatic conditions. We will follow a less general approach searching for a field in a particular form

$$E(r) = \frac{E_a \cdot r_a^n}{r^n}, \tag{3}$$

where we write explicitly the magnitude of the electric field $E(r)$ rather than U'. The parameter n, called the power of the field drop, describes the form of the field. $n = 0$ corresponds to a uniform field with 1 dimensional symmetry; $n = 1$ corresponds to the electric field around an anode wire with cylindrical symmetry; and $n = 2$ corresponds to a field having spherical symmetry. The formula is exact with r_a being the radius of the anode wire. Other values of the parameter n have only a mathematical meaning.

Our initial tests have used a gas mixture of 80% Ar and 20% CO_2. The first Townsend coefficient, α, at atmospheric pressure can be parameterized as

$$\alpha(E) = a \cdot exp(-b/E), \tag{4}$$

where $a = 1.05/\mu\text{m}$ and $b = 13.25\, V/\mu\text{m}$.[4]

Figure 1 shows results of Eq.1 with electric field given by Eq.3, α being defined in Eq.4 for three different anode radii. We see that for practical values of anode radius around 20 μm, maximum gas gain is reached for $n \approx 1.7$. This power of the field drop is close to that of a spherical geometry. A practical detector geometry generating such a field is that of a pin with a semi-spherical tip of radius r_a, within a cylindrical cathode higher than the pin. Electric field simulations show that in such a structure, n does indeed vary from about 1.9 to 1.5.

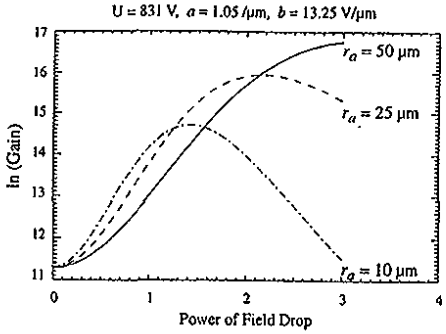

Figure 1: Natural logarithm of the gas gain as a function of the parameter n, called power of the field drop. The three curves correspond to different "anode radii" r_a. In all cases the radius of the cathode (extent of the field) is $r_c = r_a + 175\,\mu$m.

3 Prototype Electrodes

The MIPA electrodes were fabricated from SU-8, an epoxy-based, negative-acting photoresist that displays excellent transparency in the near UV. The relative UV transparency of this resist, when exposed with collimated UV radiation that minimizes lateral scattering, enables the fabrication of microstructures with vertical sidewalls and aspect ratios (sidewall height divided sidewall thickness) of 15:1. A standard chrome-on-quartz mask, typically used for lithography in integrated circuit fabrication, is used to fabricate the MIPA electrode array an SU-8 layer spun on to a silicon wafer.

Scanning electron micrographs in Figure 2 illustrates the primary fabrication steps. The anode, Figure 2a, is exposed with an initial mask to form an array of pins 50 μm in diameter and 200 μm high. After exposure and annealing, the SU-8 polymer cross-links and becomes insoluble in a developing solution that removes the unexposed material. The entire electrode array is then vacuum evaporated with gold. Then, an additional SU-8 layer is spun over the anode structure, and patterned with another mask consisting of a repeating hexagonal pattern. After development, the second SU-8 layer consists of a hexagonal honeycomb microstructure that forms the cathode, Figure 2b. Gold is vacuum deposited on the cathode, with the lower half of the structure being left uncoated to provide electrical isolation from the anode array. The full prototype consists of a 48×56 array of cells, each with an internal radius of 300 μm in the xy plane.

The position of the anode tips well below the upper plane of the cathode is the reason for the rapid change in electric field close to the tips. However, this recess may lead to a problem with full

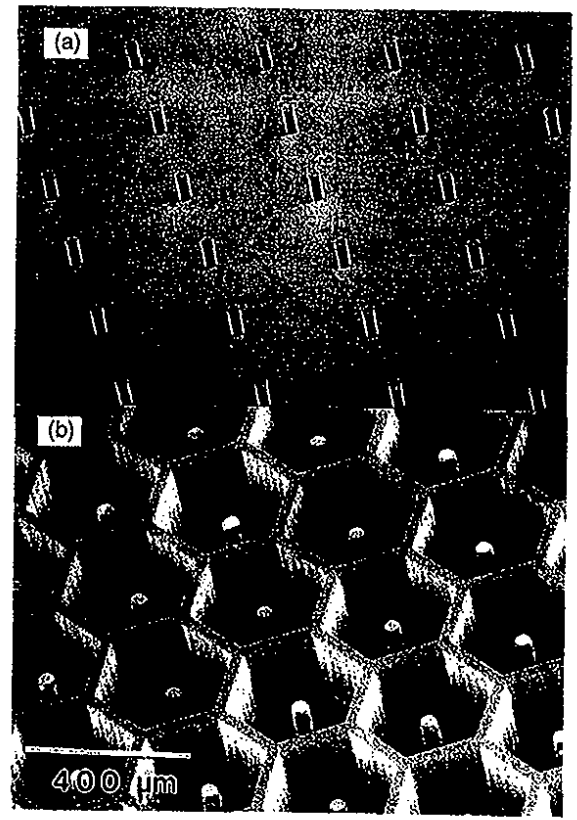

Figure 2: (a) Anode fabricated from SU-8, on silicon wafer; (b) Complete anode / cathode microstructure.

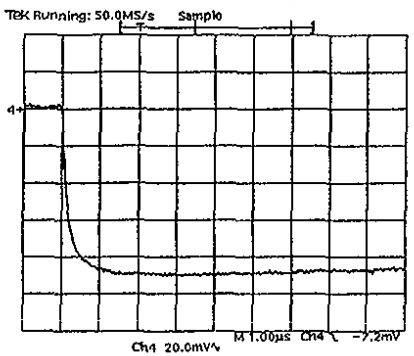

Figure 3: Signal waveform at the output of a charge sensing preamplifier connected to the cathode of the MIPA structure excited by a 5.9 keV X-ray.

collection of signal electrons produced by the X-rays in a drift volume directly above the cathode. All lines of force starting from the negatively biased window of the detector which encloses the drift volume must end on anodes, none of them on the cathode. A deeper recess of the anode tips inside the cathode structure requires a higher field in the amplification region relative to the field in the drift region. The recess chosen is a compromise between the sphericity of the amplification field (stability of operation) and full collection of electrons with a practical value of drift field. The hexagonal form of the individual cells minimizes the front surface of the cathode array as seen by signal electrons, thus improving electron collection properties of the array.

4 Experimental Results

The MIPA structure was enclosed in a box with an entrance window 1 cm above the cathode. For these initial tests all anodes were connected together and the cathode structure was left electrically undivided. A flow gas of 80% Ar and 20% CO_2 was used. The detector was operated with the cathode at ground potential, the anodes at a positive potential of several hundred volts, with the entrance window at a negative potential.

Figure 3 shows a signal waveform at the output of a charge sensing preamplifier connected to the cathode of the MIPA structure excited by 5.9 keV X-rays. An identical but inverted waveform was observed from an amplifier connected to the anodes. We see that the rise time of the integrated pulse, that is, the duration of the current signal, is about 1 μs. This corresponds to the drift time

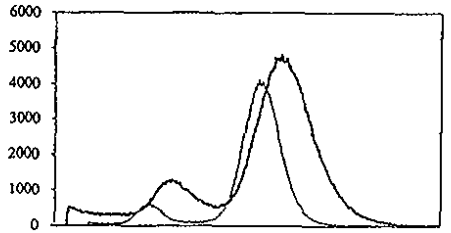

Figure 4: X-ray spectra from MIPA detector. Thin line: one or two cells illuminated by 5.4 keV X-rays. Thick line: entire prototype illuminated by 5.9 keV X-rays.

of the positive ions traversing the distance between the tip of the anode and the top plane of the cathode array.

Figure 4 shows X-rays spectra with a) only one or two cells illuminated and b) the entire array illuminated. We believe that the worsening of the energy resolution for full illumination of the detector is due to geometric imperfection of the array.

Figure 5 shows the dependence of gas gain on the anode voltage, measured with a charge sensing preamplifier followed by a 1 μs single delay line shaper. The detector can operate at a gain up to several times 10^4 without discharge.

The gas gain dependence has been studied as a function of photon rate using a collimated 5.4 keV X-ray beam. Figure 6 shows the results. At a nominal gas gain of 2400, a repeatable decrease in gain of about 10% for a rate of 10^6 X-rays $mm^{-2}s^{-1}$ was observed. This decrease may be due to the space charge, but is an acceptable decrease for most of the applications.

The geometry and the electric field of the amplification region of the MIPA detector are such that not all the positive ions created by the avalanche process return to the window. Figure 7 shows the ratio of current flowing to the entrance window (charge traversing the whole drift distance of the detector) to the current flowing to the cathode structure, as a function of the negative voltage applied to the window. The anode voltage was adjusted to maintain a constant gas gain. For small values of drift field, only about 5% of the positive ions created by avalanches return to the window. The ratio increases almost linearly with drift field. However, the drift time of positive ions within the drift region decreases with drift field. The net effect is that the density of positive charges in the drift region of the detector is, to first order, independent of drift field for constant flux and gas gain.

Figure 8 show the dependence of the 5.9 keV X-ray pulse height on the drift voltage for two different values of the gas gain. For values of drift voltage smaller than about 700 V (drift field below

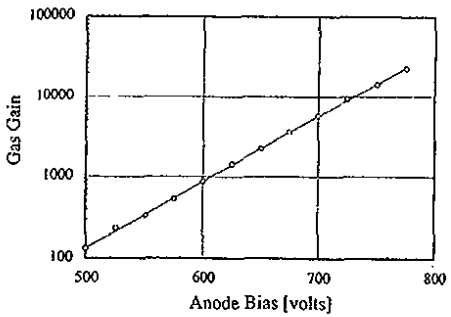

Figure 5: MIPA gas gain as a function of the anode pin bias voltage. (window at -500 V, 5.4 keV X-rays)

700 V/cm) the pulse height increases due to an increase in the electric field in the amplification region. However, a decrease in the pulse height is clearly visible once the negative voltage on the window exceeds 1000 V. The gas gain cannot decrease with higher values of electric field and our explanation is that a fraction of the primary electrons are being lost on the cathode structure of the MIPA. This hypothesis is supported by an observed worsening of the energy resolution for the higher value of drift field and also agrees with the field simulation.

5 Conclusions and Future Work

A new micro-structure for electron multiplication in gas is being developed, with the aim of overcoming electrical instabilities that have affected earlier micro-structure detectors. Initial experimental results indicate that characteristics specifically designed into the device to address this problem have succeeded.

Considerable work remains to be done. We are exploring methods to reduce geometric imperfections, fabricating structures that have anode pins with a smaller recess with respect to the top plane of the cathode, and improving our understanding of space charge effects. All these studies may improve gain uniformity. In the longer term, we are investigating methods to read-out position information either from groups of pins or from individual pins. We believe the MIPA represents a promising new detector that will have uses extending beyond its primary purpose in time-resolved X-ray crystallography.

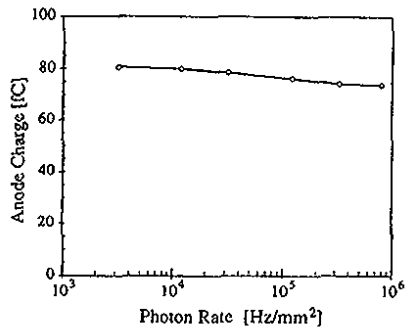

Figure 6: Anode charge as a function of photon rate with a collimated 5.4 keV X-ray beam. The beam size is 25 μm $\times$ 1 mm.

6 Acknowledgements

The authors wish to thank E.F. Von Achen and D.C. Elliott for assistance with the detector development.

References

[1] P. Rehak, G.C. Smith and B. Yu, "A Method for Reduction of Parallax Broadening in Gas-Based Position Sensitive Detectors," *IEEE Trans. Nucl. Sci.*, 44 (1997) 651-655

[2] A. Bressan et al, "High Rate Behavior and Discharge Limits in Micro-Pattern Detectors," *Nucl. Instrum. and Meth.* A424 (1999)321-342

[3] C. Richter,"Microstrip-Gas-Chambers for the HERA-B Experiment," Proceedings of the International Workshop on Micro-Pattern Detectors, Orsay, France, June 28-30, 1999

[4] J.C. Armitage et al., "A Study of the Effect of Methane and Carbon Dioxide Concentration on Gas Amplification in Argon Based Gas Mixtures," *Nucl. Instrum. and Meth.*, A271 (1988) 588-596

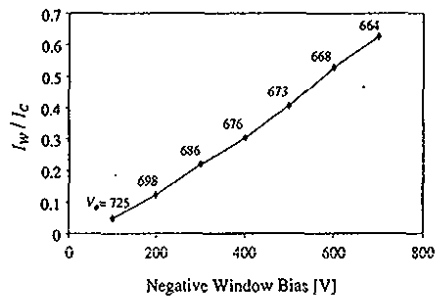

Figure 7: Ratio of current of positive ions returning to the entrance window and current of ions flowing into the cathode as a function of the negative window voltage.

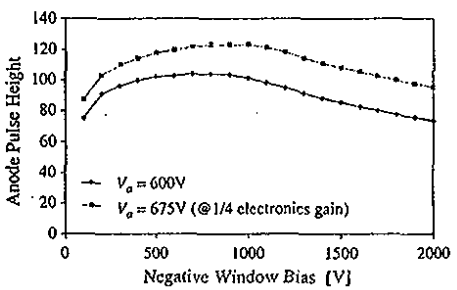

Figure 8: Pulse height of monochromatic X-rays as a function of the bias applied on the entrance window for two different anode voltages.